European Journal of
Mineralogy
Open Access

Metamorphic titanite–zircon pseudomorphs after igneous zirconolite

Cindy L. Urueña, Charlotte Möller, and Anders Plan

Department of Geology, Lund University, Lund, 223 62, Sweden

Correspondence: Cindy L. Urueña (cindy.uruena@geol.lu.se)

Abstract. The formation of metamorphic zircon after baddeleyite is a well-known reaction that can be used to date the metamorphism of igneous silica-undersaturated rocks. By contrast, metamorphic minerals formed after igneous zirconolite have rarely been reported. In this paper, we document metamorphic titanite + zircon pseudomorphs formed from the metamorphic breakdown of igneous zirconolite in syenodiorite and syenite, in the southeastern Sveconorwegian Province, Sweden. Water-rich fluid influx during tectonometamorphism in epidote–amphibolite-facies metamorphic conditions caused the release of silica during a metamorphic reaction involving igneous feldspar and pyroxene and the simultaneous breakdown of igneous Zr-bearing phases. Typical titanite + zircon intergrowths are elongated or platy titanite crystals speckled with tiny inclusions of zircon. Most intergrowths are smaller than 15 µm; some are subrounded in shape. Locally, bead-like grains of titanite and zircon are intergrown with silicate minerals. The precursor igneous zirconolite was found preserved only in a sample of near-pristine igneous syenodiorite, as remnant grains of mainly < 2 µm in size. Two somewhat larger crystals, 8 and 12 µm, allowed semiquantitative confirmation using microprobe analysis. Analogous with zircon pseudomorphs after baddeleyite, titanite + zircon pseudomorphs after zirconolite potentially offer dating of the metamorphic reaction, although the small size of the crystals makes dating with today's techniques challenging. The scarcity of reports of zirconolite and pseudomorphs reflects that they are either rare or possibly overlooked.

1 Introduction

In continental crust, metamorphic recrystallisation of H_2O-poor igneous rocks is commonly steered by the influx of hydrous fluid, often guided by deformation (Austrheim, 1987; Engvik et al., 2000, 2001; Menegon et al., 2017). Metamorphism is, therefore, typically heterogeneously developed even in the deep parts of orogens (e.g. Austrheim, 2013; Jamtveit et al., 2018; Möller and Andersson, 2018; and, in this special issue, Gyomlai et al., 2023). The unreacted (metastable) igneous rocks and gradual transitions to metamorphosed equivalents allow insights into the progress of metamorphic reactions. In some silica-undersaturated gabbroic rocks, the metamorphic reaction and, by implication, the influx of hydrous fluid and associated deformation can also be dated. This is, for example, possible for metagabbro in which the silica released from the metamorphic reactions has led to the replacement of baddeleyite (ZrO_2) by metamorphic zircon ($ZrSiO_4$; Davidson and van Breemen, 1988; Beckman and Möller, 2018).

While zircon growth after baddeleyite is a comparably well-known reaction (Davidson and van Breemen, 1988), there are to this date only a few reports (Pan, 1997; Pohlner et al., 2020) of metamorphic mineral growth after zirconolite, $CaZrTi_2O_7$. This may be due to zirconolite and pseudomorphs after zirconolite being either extremely rare or, possibly, overlooked. This paper documents, using electron and cathodoluminescence imaging, metamorphic titanite + zircon intergrowths formed from the metamorphic breakdown of igneous zirconolite in metamorphosed varieties of syenodiorite and syenite from the Sveconorwegian Province in southwestern Sweden. Zirconolite was found in the best-preserved igneous syenodiorite only, as remnant igneous grains of mainly very small size (< 2 µm); two larger crystals, 7 and 12 µm large, were analysed by wavelength-

dispersive X-ray spectroscopy (WDS) analysis and electron backscatter diffraction (EBSD).

2   Background

2.1   Silica-undersaturated Zr minerals

Zirconium-bearing oxides are commonly associated with silica-undersaturated rocks, offering the possibility of dating mafic rocks (Heaman and LeCheminant, 1993). The Zr oxides may crystallise and co-precipitate in different chemical environments (Carlier and Lorand, 2008). The magmatic precipitation of Zr-rich accessory minerals generally occurs at the late stage of crystallisation of deuteric fluids and melts saturated in CaO and TiO_2 (Carlier and Lorand, 2008; Della Ventura et al., 2000). The very last liquid fraction fractionates baddeleyite when SiO_2 has been depleted, but Zr, Hf, Nb, Fe^{3+}, and rare earth elements (REEs) still remain in the melt (Carlier and Lorand, 2008). Baddeleyite is the most common Zr oxide and a stable accessory mineral in Si-poor alkaline and non-alkaline igneous rocks with high Zr contents (e.g. olivine-bearing gabbroic rocks, anorthosites, alkali gabbro, nepheline syenites, kimberlites; Heaman and LeCheminant, 1993).

Zirconolite ($CaZrTi_2O_7$) is a rare accessory mineral that crystallises in silica-undersaturated and alkaline rock types and is hardly ever reported in silica-saturated rocks (e.g. De Hoog and Van Bergen, 2000). Zirconolite-bearing rocks include kimberlites, carbonatites, layered intrusions, anorthosites, nepheline syenite, metasomatic rocks, metamorphic rocks, placer deposits, and non-terrestrial materials such as chondrites and lunar rocks (Williams and Gieré, 1996; Gieré et al., 1998; Rasmussen and Fletcher, 2004). Metamorphic zirconolite has also been reported to result from partial anatexis of ultrahigh-temperature sapphirine granulite in Antarctica (Harley, 1996) and has been related to metasomatism of carbonates during contact metamorphism (e.g. Tropper et al., 2007; Purtscheller and Tessadri, 1985; Williams and Gieré, 1988; Gieré, 1986). The formation of zirconolite depends on the silica activity such that SiO_2- and CO_2-bearing fluids may destabilise zirconolite (Tropper et al., 2007; Gieré et al., 1998; Spiridonov et al., 2019). Zirconolite is commonly associated or forms intergrowths with other Zr-bearing oxides, such as baddeleyite, calzirtite ($Ca_2Zr_5Ti_2O_{16}$), srilankite (Ti_2ZrO_6), and zircon (Gieré et al., 1998; Spiridonov et al., 2019).

Calzirtite is infrequent and is characteristic of alkalic and ultramafic complexes associated with carbonatites. Srilankite is considered a high-temperature polymorph of a disordered Zr-titanate solid solution; it has been reported from mantle xenoliths, ultramafic diatremes, and crustal mafic granulites (Bingen et al., 2001; Troitzsch et al., 2005).

2.2   Zirconolite polytypes and crystal chemistry

The crystal structure of zirconolite is described as a layer structure analogous to the pyrochlore (Mazzi and Munno, 1983; Gieré et al., 1998) and to an anion-deficient fluorite structure type (Pyatenko and Pudovkina, 1964; Gieré et al., 1998). The zirconolite structure consists of alternate layers of TiO_6 polyhedra aligned parallel to (001) with Zr^{4+} and Ca^{2+} arranged in planes (010) and (100), respectively. The complexity of the structure increases with the incorporation of trivalent REEs (e.g. La^{3+} and Nd^{3+}) and tetravalent elements U and Th (Nickolsky and Yudintsev, 2021; Rasmussen and Fletcher, 2004). Furthermore, zirconolite may crystallise in three different systems; the varieties are known as polytypes and include zirconolite-*3O* (three-layered orthorhombic polytype), zirconolite-*3T* (three-layered trigonal polytype), and zirconolite-*2M* (two-layered monoclinic polytype). Zirconolite without a suffix denotes non-crystalline (metamict) zirconolite. The cubic variety is named zirkelite (Bayliss et al., 1989; Nickolsky and Yudintsev, 2021; Rasmussen and Fletcher, 2004).

Stoichiometric zirconolite with the formula $CaZrTi_2O_7$, commonly doubled to $Ca_2Zr_2Ti_4O_{14}$, contains 16.5 wt % CaO, 36.3 wt % ZrO_2, and 47.2 wt % TiO_2 (Williams and Gieré, 1996; Gieré et al., 1998). The composition of zirconolite is described in a composition space with five endmembers (Table 1; Haifler et al., 2021).

Variations in the zirconolite composition are controlled by the bulk chemical environment. The crystal structure allows extensive substitutions in five cation sites that permit great flexibility in the ionic radius (0.40 to 1.14 Å) and charge (2+ to 6+) of chemical species (Williams and Gieré, 1996; Gieré et al., 1998; Rasmussen and Fletcher, 2004). The major replacements are trivalent REEs and tetravalent actinides for ^{VIII}[Ca]; Nb and Ta for ^{VI}[Ti]; Fe, Mg, or Al for $^{IV V}$[Ti]; and Hf for ^{VII}[Zr] (Gieré et al., 1998; Bayliss et al., 1989). Subordinate quantities of other elements can be incorporated in the same crystallographic sites – for instance, divalent cations (i.e. Mn^{2+} or Mg^{2+}) may occupy octahedral sites (Della Ventura et al., 2000; Chukanov et al., 2014, 2019). Iron and Al^{3+} may occupy the $^{IV V}$[Ti] sites, but, at high Fe content, Fe is accommodated in two distinct octahedral sites (Mazzi and Munno, 1983; Zubkova et al., 2018; Chukanov et al., 2019, 2018, 2014; Haifler et al., 2021).

3   Analytical methods

Microtextural documentation and mineral identification were performed on polished thin sections by using a Tescan MIRA3 field emission scanning electron microscope (FE-SEM) coupled with an Oxford Instruments energy-dispersive X-ray spectroscopy (EDS) analysis system and a cathodoluminescence (CL) imaging system at the Department of Geology, Lund University. Operation conditions

Table 1. Zirconolite endmembers proposed by Haifler et al. (2021), and the equivalent cationic substitution from the ideal formula $Ca_2Zr_2Ti_4O_{14}$. $ACT = Th + U$; $Me^{5+} = Nb \pm Ta$; $Me^{2+} = Fe^{2+} \pm Mg$; $Me^{3+} \approx Fe^{3+}$, other trivalent cations.

Zirconolite endmember	Cationic substitution
$Ca_2Zr_2Me_2^{5+}TiMe^{2+}O_{14}$	$3\,Ti^{4+} \leftrightarrow 2\,Me^{5+} + Me^{2+}$
$REE_2Zr_2Ti_3Me^{2+}O_{14}$	$2\,Ca^{2+}\,Ti^{4+} \leftrightarrow 2\,REE^{3+} + Me^{2+}$
$CaACTZr_2Ti_3Me^{2+}O_{14}$	$Ca^{2+}\,Ti^{4+} \leftrightarrow ACT^{4+} + Me^{2+}$
$CaREEZr_2Ti_3Me^{3+}O_{14}$	$Ca^{2+}\,Ti^{4+} \leftrightarrow REE^{3+} + Me^{3+}$
$Ca_2Zr_2Ti_2Me^{5+}Me^{3+}O_{14}$	$2\,Ti^{4+} \leftrightarrow 2\,Me^{5+} + Me^{3+}$

follow the standard method of the laboratory: accelerating voltage at 15 kV, beam diameter at 1 µm, and a counting time of 60 s. The identification and/or compositional analysis of all minerals in the samples was made by EDS, using AZTEC software by Oxford Instruments. The element setup for wavelength-dispersive electron microprobe (WDS-EMPA) analysis of zirconolite was based on the results from the EDS analyses.

For the mineral chemistry of zirconolite (two $\leq 12\,\mu m$ large crystals), quantitative analysis was performed in situ in a thin section using the JEOL JXA-8230 electron probe microanalyser (EPMA) at the Universidad Nacional de Colombia. Major and trace elements were collected with a 1 µm diameter beam, 20 nA current, acceleration voltage at 15 kV, and 20 s collection time on the peak with background counting times of 10 s for Al, Nb, Lu, Gd, Eu, Pr, and Ce and 5 s for all other elements. The acquisition time was restricted to minimise the beam damage effects on the small zirconolite crystals, which limited the analytical resolution. Detection limits for Y + REE ranged from 300 to 1000 ppm. The X-ray lines and standards used during the WDS analysis counts are summarised in Table 2. Several trial-and-error tests were made to define the interferences at which the analysis gave the best fit. Peak overlap corrections were applied for the interferences Eu–Pr and Er–Tb. For correction of background interferences, the spectrometer was set to measure count rates on both sides of the peak and on one side for Al, Nb, Lu, Gd, Eu, Pr, and Ce. The respective counts were converted to weight percentage oxides applying the CitZAF correction method. Fe^{3+} was calculated by stoichiometry following the general equation by Droop (1987).

For the purpose of determining the crystallographic properties, we attempted to analyse the largest (12 µm) zirconolite crystal using electron backscattered diffraction (EBSD). However, the results of the EBSD analysis were not conclusive (data provided in Supplement).

4 Geological context

The rocks investigated in this study are part of the Vaggeryd syenite complex in southern Sweden. The Vaggeryd syen-

ite complex is a N–S elongated body about 50 km long and 7 km wide, which intruded at 1.22 Ga (Pb–Pb ages from single zircon evaporation; Ask, 1996; Fig. 1). The main rock is syenite, but other silica-poor rocks, e.g. quartz syenite, mangerite, charnockite, and leucogabbro, also occur. The Vaggeryd syenite complex is located within the easternmost part of the Eastern Segment of the Sveconorwegian orogen, the remnant of a 1 Ga, large, and hot orogen at the southwestern margin of the Fennoscandian Shield (Fig. 1a). The Vaggeryd syenite complex is heterogeneously deformed by numerous N–S-striking ductile shear zones (Söderlund and Ask, 2006) that have also deformed the surrounding host rocks (Fig. 1b). Similarly aged granitic and syenitoid intrusions are also present further west in the Sveconorwegian Province, within the Eastern Segment (Fig. 1a), in areas that were metamorphosed under higher-grade conditions.

The Eastern Segment is dominated by granitic rocks, originally generated inside of a Paleoproterozoic convergent margin, and was later metamorphosed and reworked during the 1.4 Ga Hallandian and 1.0 Ga Sveconorwegian orogenies (Möller et al., 2015; Piñán-Llamas et al., 2015; Ulmius et al., 2015; Möller and Andersson, 2018; Stephens et al., 2020). The main rock types include 1.73–1.67 Ga granite, granodiorite, and quartz monzodiorite (and subordinate volcanic rocks), and also there are lesser amounts of 1.40–1.45 Ga granite and syenite and 1.22 Ga syenodiorite and monzonorite with associated basic intrusives as the product of bimodal magmatism (Fig. 1b; Söderlund and Ask, 2006). Dolerite dykes intruded at ca. 1.56, 1.22, and 0.96 Ga (Söderlund et al., 1999, 2005; Johansson et al., 2001).

The Eastern Segment records the latest Sveconorwegian collisional stage at 990–960 Ma, during which it was overthrust by Sveconorwegia (Fig. 1). This event resulted in westward-increasing metamorphic grade from epidote–amphibolite facies to high-pressure granulite facies within the Eastern Segment and the exhumation of an eclogite terrane beneath the contact with Sveconorwegia. The easternmost boundary of the Sveconorwegian Province, in which the Vaggeryd syenite complex is situated, is a ca. 25 km wide subvertical N–S-trending deformation zone, progressively changing eastwards into discrete steeply west-dipping shears (the Frontal wedge in Fig. 1a, b; Wahlgren et al., 1994; Möller and Andersson, 2018). The steep structures in the Frontal wedge mark the eastward-waning ductile deformation and recrystallisation in the deeply buried Eastern Segment during the Sveconorwegian orogeny. Lithologies are continuous across this zone, which shows that the Frontal wedge is an intraplate deformation structure (Söderlund and Ask, 2006; Möller et al., 2015; Möller and Andersson, 2018). The ductile deformation within the Frontal wedge was nonpenetrative and associated with metamorphic recrystallisation under epidote–amphibolite- to greenschist-facies conditions. In many places, rocks remain in a pristine igneous or pre-Sveconorwegian state (Möller and Andersson, 2018).

Table 2. Analytical setup and calibration standards used for the electron microprobe analyses of zirconolite.

Element	Line	Peak position (mm)	Spectrometer crystal	Standard
Mg	$K\alpha$	107.558	TAP	Periclase
Al	$K\alpha$	90.771	TAP	Orthoclase
Si	$K\alpha$	77.664	TAP	Orthoclase
Ca	$K\alpha$	107.961	PETJ	Wollastonite
Ti	$K\alpha$	88.678	PETJ	Titanite
Fe	$K\alpha$	134.732	LIFH	Hematite
Y	$L\alpha$	206.563	PETH	YAG
Zr	$L\alpha$	194.339	PETH	Zircon
Nb	$L\alpha$	183.302	PETJ	Niobium (metal)
La	$L\alpha$	185.421	LIFH	LaF_3
Ce	$L\alpha$	178.185	LIFH	$CeAl_2$
Pr	$L\alpha$	171.376	LIFH	PrF_3
Nd	$L\alpha$	164.921	LIFH	NdF_3
Sm	$L\alpha$	153.083	LIFH	SmF_3
Eu	$L\alpha$	147.595	LIFH	EuF_3
Gd	$L\alpha$	142.404	LIFH	GdF_3
Dy	$L\alpha$	132.868	LIFH	DyF_3
Ho	$L\alpha$	128.357	LIFH	HoF_3
Er	$L\alpha$	124.205	LIFH	ErF_3
Tm	$L\alpha$	120.237	LIFH	$TmSi_2$
Yb	$L\alpha$	116.348	LIFH	Synthetic glass
Lu	$L\alpha$	112.763	LIFH	$LuSi_2$

4.1 Sample site

In a quarry at Näsbyholm in the southernmost part of the Vaggeryd intrusion (Fig. 1b), syenitoid rocks are well-exposed in outcrops along a ca. 250 m E–W section. The main rock has local compositional variations spanning from reddish feldspar-rich syenite to dark melanocratic syenodior-ite (probably incomplete mixing between syenitic and gab-broic melts). This main syenitoid complex also hosts metre-wide diabase and pegmatite dykes. All rock types have been heterogeneously overprinted by deformation and associated metamorphism with strain variations over distances of less than a metre. Locally, undeformed rocks are medium- to coarse-grained with crystal sizes up to 1 cm, preserving their igneous fabrics. Where deformed, the rocks are foliated and recrystallised into metamorphic minerals of fine grain size (< 0.5 mm). Although the overall orientation of the folia-tion is interpreted to align with the regional N–S subverti-cal trend, the foliation anastomoses in different directions around lens-shaped domains on the scale of a few metres (Fig. 1c).

4.2 Sampling

Samples were taken within ca. 100 m of the same quarry out-crop. A well-preserved coarse-grained melanocratic syenodi-orite was found in one spot only, in a domain a few me-tres large, surrounded by recrystallised syenodiorite transi-tioning from weakly deformed to mylonite. Figure 2a and b illustrate the difference between a well-preserved melano-cratic syenodiorite, in this paper referred to as near-pristine igneous syenodiorite, and a weakly to moderately deformed and recrystallised variety of the same rock. The samples in-vestigated in this study are mainly of syenodioritic compo-sition (the bulk rock chemistry for three samples is provided in the Supplement, Table S1), but one sample is more red-dish, dominated by alkali feldspar, and of syenitic compo-sition. The syenodioritic samples include variations in the degree of strain and associated metamorphic recrystallisa-tion; the reddish syenitic sample is strongly deformed. Five thin sections of the melanocratic syenodiorite, as well as one deformed alkali-feldspar-dominated syenite (09h), were in-vestigated for Zr-bearing accessory minerals. Of these, one sample is near-pristine igneous syenodiorite (09j), one is a metamorphosed and undeformed variety (09a), and the four remaining samples are metamorphosed and deformed (09b, 09c, 09g, and 09h).

5 Results

5.1 Petrography

The near-pristine igneous syenodiorite is dominated by dark-grey plagioclase crystals mantled by mesoperthite and an in-terstitial aggregate of dark minerals consisting of orthopyrox-
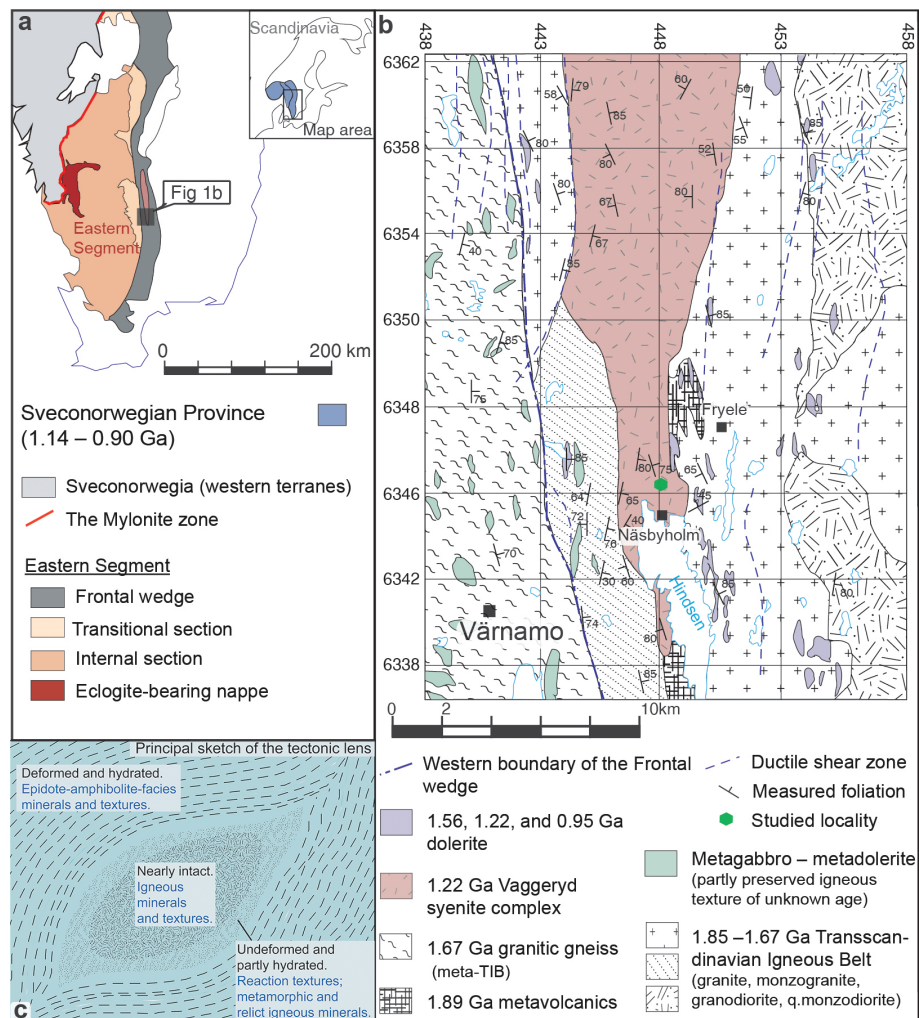
Figure 1. Tectonic and geological setting. **(a)** Simplified tectonic map of the Sveconorwegian Province with the internal subdivision of the Eastern Segment (Möller et al., 2015). The Vaggeryd syenite complex is located within the Frontal wedge and shown in reddish-brown. **(b)** Overview bedrock map of the southern part of the Vaggeryd syenite complex and surroundings (based on a 1 : 250 000 scale database), including previously unpublished structural data from Rikard Ask. The studied locality north of Näsbyholm is marked with a green spot (source: map viewer Geological Survey of Sweden, SGU; coordinate system: SWEREF 99; meta-TIB: metamorphosed Transscandinavian Igneous Belt rocks). **(c)** Sketch illustrating progressive changes in deformation and metamorphic recrystallisation in the studied syenodiorite, with the near-pristine igneous rock preserved in the core of a lens with weakly to moderately deformed and metamorphosed margins.

ene crystals and lesser amounts of opaques, clinopyroxene, and biotite (Fig. 2a, c). In the deformed varieties, the feldspar occurs as augen or porphyroclasts, wrapped by biotite-rich folia, and pyroxenes are absent (Fig. 2b, d).

Igneous syenodiorite. In the near-pristine igneous syenodiorite, a mesoperthitic mantle (Fig. 2e–f) surrounds coarse plagioclase crystals. These feldspars are oligoclase–andesine (An_{32} to An_{34}, with an orthoclase component of up to 1 %) and alkali feldspar. The composition of the exsolved alkali-feldspar phase in mesoperthite is Or_{68-91} Ab_{9-27}. The aggregates of ferromagnesian phases (Fig. 2e–f) consist of coarse-grained orthopyroxene with exsolution lamellae of calcic pyroxene (the latter 15 vol %) and lesser amounts of bi-

otite, apatite, and Fe–Ti oxides. Accessory minerals include titanomagnetite (magnetite with ilmenite lamellae), ilmenite, sulfides, baddeleyite, zircon, and zirconolite (detailed below). A few grains of srilankite were also found as minute inclusions in feldspar and baddeleyite grains. Small crystals of metamorphic minerals were also identified: tiny epidote–clinozoisite inclusions ($\sim 50\,\mu m$ in size) in plagioclase and thin rims of very fine-grained biotite on orthopyroxene crystals.

Metamorphosed syenodiorite. The recrystallised and deformed equivalent of the melanocratic syenodiorite (Fig. 2b, d, g, h) is made up of sodic plagioclase (An_{3-17}), K-feldspar, biotite, epidote–clinozoisite, quartz, garnet, titanite,
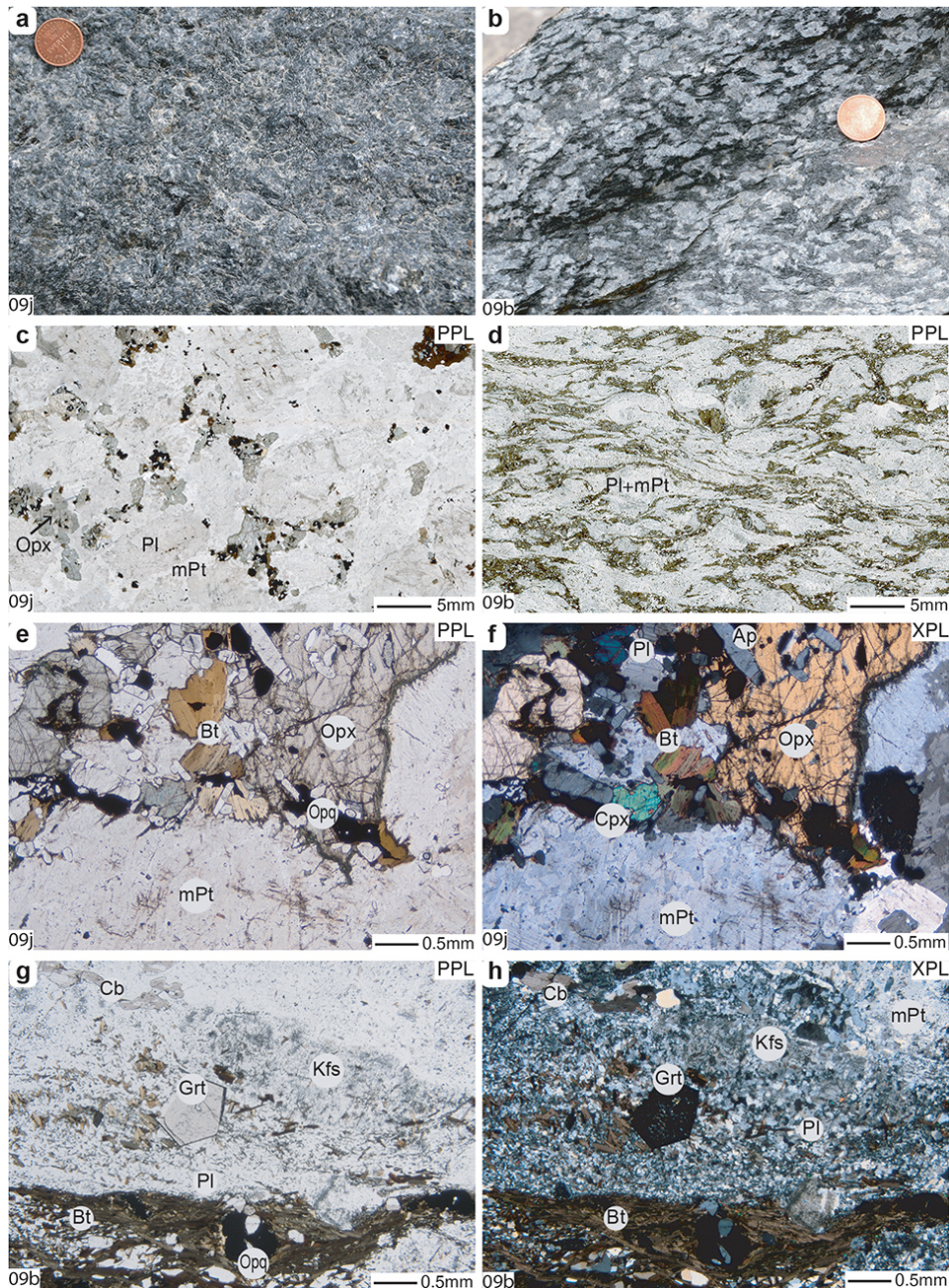
Figure 2. Mineralogical and textural differences between the igneous syenodiorite **(a, c, e–f)** and its hydrated, metamorphosed, and deformed equivalents **(b, d, g–h)**, including field appearance, scanned thin sections, and photomicrographs (PPL, plane polarised light; XPL, cross-polarised light). Mineral abbreviations follow Whitney and Evans (2010): Ap, apatite; Bt, biotite; Cb, carbonate; Cpx, clinopyroxene; Grt, garnet; Kfs, K-feldspar; mPt, mesoperthite; Opq, opaque phase; Opx, orthopyroxene; Pl, plagioclase. **(a)** Dark-grey, coarse-grained orthopyroxene syenodiorite, representative of the near-pristine igneous rock, to be compared with **(b)**. **(b)** Metamorphosed, weakly to moderately deformed, and almost completely recrystallised syenodiorite. **(c)** Thin-section overview of near-pristine igneous syenodiorite made up of igneous plagioclase rimmed by mesoperthite, orthopyroxene, minor biotite, and Fe–Ti oxides, to be compared with **(d)**. **(d)** Thin-section overview of deformed syenodiorite with porphyroclasts of igneous feldspar (plagioclase and mesoperthite) and elongated aggregates of metamorphic dark minerals (dominantly biotite). **(e–f)** Photomicrographs (detail) of the near-pristine igneous syenodiorite **(a, c)**, illustrating irregular mesoperthitic feldspar intergrowths and an aggregate of mainly ferromagnesian igneous phases: coarse orthopyroxene crystals, subordinate clinopyroxene, biotite, opaque minerals, and apatite. The igneous pyroxene crystals have thin rims of very fine-grained metamorphic biotite, indicative of incipient metamorphism. **(g–h)** Photomicrographs (detail) of the metamorphosed and moderately foliated syenodiorite **(b, d)**. A fine-grained biotite-rich foliation trail is seen in the lower part of the photos. Above is a fine-grained aggregate of recrystallised plagioclase with a euhedral garnet crystal and, at the top of the images, relict igneous mesoperthite. Sub-microscopic (10–30 μm) epidote–clinozoisite grains occur in all three domains (seen in Fig. 4).

and calcite. All deformed and metamorphosed varieties of the melanocratic syenitoid are devoid of pyroxene. Sodic plagioclase predominantly forms fine-grained granoblastic aggregates, together with quartz and biotite in lens-shaped and flattened domains (Fig. 2b, d). Locally, coarse-grained mesoperthitic microstructures are still present in the cores of the feldspar domains, as remnants of the igneous feldspar. The ductile deformation fabric is defined by lensoid and flattened feldspar domains, thin and long dark mineral aggregates, and oriented biotite flakes (Fig. 2d, g–h). Fine-grained aggregates of metamorphic epidote–clinozoisite and carbonate are distributed within the felsic domains. Idiomorphic garnet crystals are present locally, containing inclusions of epidote–clinozoisite and quartz. The absence of strain shadows or deflection of the external foliation around garnet porphyroblasts, as well as the inclusion trails being continuous with the matrix foliation, indicate a late-tectonic or post-tectonic formation of the garnet.

5.2 Zirconium phases and their microtextural relationships

The accessory Zr phases in the near-pristine igneous syenodiorite are different from those in the metamorphosed varieties. Zirconolite and baddeleyite are present only in the near-pristine igneous variety, while the titanite–zircon pseudomorphs have formed solely in the recrystallised rocks. Below, we report the textural appearance of these different Zr phases. Metamorphic and igneous zircon crystals can be differentiated based on their shape and zoning (briefly described below); they have been dated and chemically characterised by SIMS (secondary ion mass spectrometry; these data are reported in Urueña and Möller, 2023).

Igneous baddeleyite. This is preserved only in the near-pristine igneous syenodiorite (sample 09j). Most baddeleyite crystals range in size from 20 to 100 μm. The baddeleyite blades are anhedral and commonly have up to 5 μm wide zircon rims (Fig. 3a). These zircon rims on baddeleyite are likely metamorphic, but a late igneous origin cannot be excluded based on the textural relationship only.

Igneous zircon. This occurs randomly in both near-pristine and metamorphosed varieties of syenodiorite and syenite; in sample 09g, it is abundant. The igneous zircon crystals have prismatic or anhedral shapes (some are fractured). Under CL, zircon crystals show either broadband oscillatory zoning (09a, 09b, 09c, 09h, 09j; Fig. 3b) or a convoluted zoning pattern with apparent flow structure (09g; typical of igneous zircon in syenitoids; e.g. Andersson, 2012).

Metamorphic zircon. This is abundant in all samples of metamorphosed and recrystallised syenodiorite. Unlike igneous zircon, metamorphic zircon typically forms irregular crystals and/or aggregates with a "multi-nuclei" texture (Fig. 3c), commonly referred to as "polycrystalline" (e.g. Beckman and Möller, 2018, and references therein). The in-

ner nucleus of each zircon grain is the most luminescent (Fig. 3c).

Zirconolite. This is rare and was found as very small grains only, commonly < 5 μm, in the near-pristine igneous syenodiorite only (sample 09j). The largest two zirconolite crystals are euhedral prismatic to subhedral, up to 12 μm long and 5 μm wide (Fig. 3d). All zirconolite grains are hosted in mesoperthitic feldspar, which commonly also contains small (inferred metamorphic) epidote–clinozoisite crystals. In places, zirconolite contains baddeleyite inclusions, indicating that baddeleyite crystallised before or simultaneously with zirconolite. The zirconolite crystals show low luminescence without internal microstructures (i.e. suggesting no zoning) and lower brightness than baddeleyite in backscattered electron images. The small zirconolite crystals appear pristine without cracks or alteration signs.

Titanite–zircon intergrowths. We interpret these to be pseudomorphs after zirconolite (see Sect. 6), and they are the main focus of this study. Figure 4 shows textural variations among these intergrowths and illustrates their appearances in secondary electron (SE), backscatter electron (BSE), and CL imagery. Titanite–zircon intergrowths are mainly hosted within feldspar domains; only a few were identified next to thin biotite foliae. Elongate or platy titanite crystals "speckled" by abundant tiny inclusions of zircon, < 2 μm large (Fig. 4a), are the most characteristic type of intergrowth. The titanite–zircon intergrowths may also be subrounded in shape (Fig. 4b). In places, the intergrowths have zircon preferentially located within the titanite core and along its rim (Fig. 4b). Titanite–zircon intergrowths were found mainly in metamorphosed syenodiorite but also within metamorphosed alkali-feldspar-dominated syenite (Fig. 4c). Typically, the intergrowths are spatially associated with fine-grained epidote–clinozoisite (Fig. 4a–c; presumably of metamorphic origin). Locally, bead-like, tiny (< 5 μm) grains of titanite and zircon are intergrown with albitic plagioclase and epidote–clinozoisite (Fig. 4d). Other titanite–zircon intergrowths appear to have undergone incipient recrystallisation/ripening, forming two distinct domains of slightly larger size (Fig. 4e); however, the zircon is still of multi-nuclei type.

5.3 Zirconolite: mineral and crystal chemistry

The intergrowths of titanite and zircon point to a precursor mineral rich in Ti, Ca, and Zr, suggesting that zirconolite is the most likely candidate. Indeed, tiny crystals with EDS spectra matching zirconolite were found in the near-pristine igneous syenodiorite. We attempted to prove that this phase is zirconolite using WDS and EBSD. Only two small crystals were large enough to analyse (> 5 μm). Three quantitative WDS analyses of these two crystals indicate a relatively limited compositional variation between the REE components: the one crystal large enough (12 μm) to allow the analysis of both core and rim indicates no compositional variation (Fig. 5, Table 3). Even though total sums are below
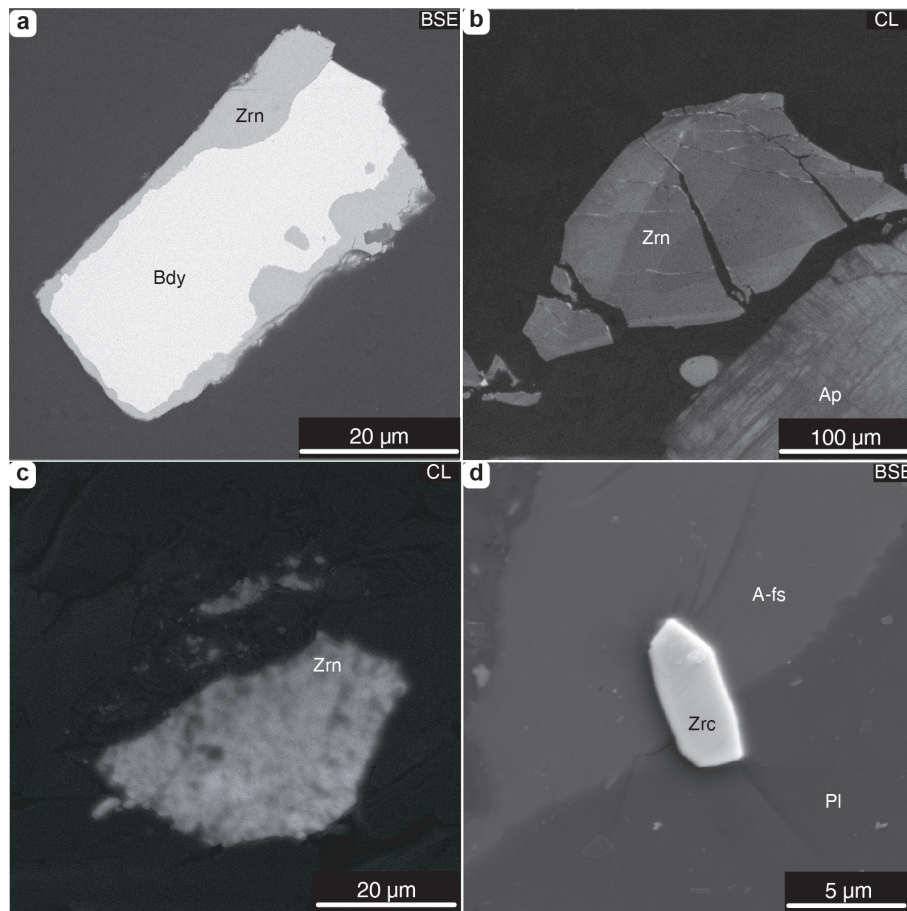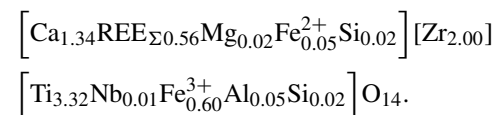
Figure 3. Backscatter electron (BSE) and cathodoluminescence (CL) images of Zr-rich minerals in the syenodiorite. Abbreviations follow Whitney and Evans (2010): A-fs, alkali feldspar; Ap, apatite; Bdy, baddeleyite; Pl, plagioclase; Zrc, zirconolite; Zrn, zircon. **(a)** Partly resorbed baddeleyite crystal with a rim of zircon (in sample 09j). **(b)** Fractured igneous zircon crystal with broadband oscillatory zoning (in sample 09a). **(c)** Metamorphic polycrystalline (multi-nuclei) zircon (in sample 09b). **(d)** Zirconolite crystal hosted in a mesoperthite (A-fs and Pl, in sample 09j).

100 %, the measured weight percentage of each oxide ranges within the average content reported for natural zirconolites in syenitoid intrusions (cf. Williams and Gieré, 1996). Low totals appear to be common for natural zirconolite, and normalised analyses have been reported (cf. Wang et al., 2021; Williams and Gieré, 1988; Carlier and Lorand, 2008). The low totals in the zirconolite analysed in this study may presumably reflect the presence of elements that were not possible to detect during the elemental identification of the small-sized zirconolite. More importantly, the proportions of constituent elements fit the composition of zirconolite.

Like most natural zirconolite, the analysed phase in this study deviates from the ideal zirconolite composition, $Ca_2Zr_2Ti_4O_{14}$. Its mineral chemistry approaches an intermediate composition between the REE endmember, $REE_2Zr_2Ti_3Me^{2+}O_{14}$, of Haifler et al. (2021; Table 1) and stoichiometric zirconolite, $Ca_2Zr_2Ti_4O_{14}$. The results suggest partial substitutions of REE by Ca^{2+}; subordinate amounts of Mg^{2+}, Al^{3+}, and Si^{4+} filling vacancies in the

structure; and a significant Fe content (most of which substitutes for Ti^{4+} in site [V]M). The most abundant REEs are (in decreasing order of abundance) Y, Ce, and Nd, but one crystal has a higher amount of Ce and lower Y and Nd. An empiric formula for analysis Zrc 24_2 (Table 3; chosen for its highest oxide sum and consistent REE pattern; see Supplement, Fig. S1) was calculated based on 8 cations and 14 oxygen atoms:

$$\left[Ca_{1.34}REE_{\Sigma 0.56}Mg_{0.02}Fe_{0.05}^{2+}Si_{0.02}\right][Zr_{2.00}]$$

$$\left[Ti_{3.32}Nb_{0.01}Fe_{0.60}^{3+}Al_{0.05}Si_{0.02}\right]O_{14}.$$

Following the crystal-chemistry models described for the zirconolite endmember $CaREEZr_2Ti_3Me^{3+}O_{14}$ (Haifler et al., 2021), $^{VIII}Ca_2^{VII}Zr_2^{VI}Ti_3^{V}TiO_{14}$ (Bayliss et al., 1989), and stefanweissite $(Ca, REE)_2 (Zr, Hf, Mn)_2 (Ti, Nb)_2 (Nb, Ti) Fe^{2+}O_{14}$ (Chukanov et al., 2019), the components in crystallographic sites for this study were allocated as follows: Ca,
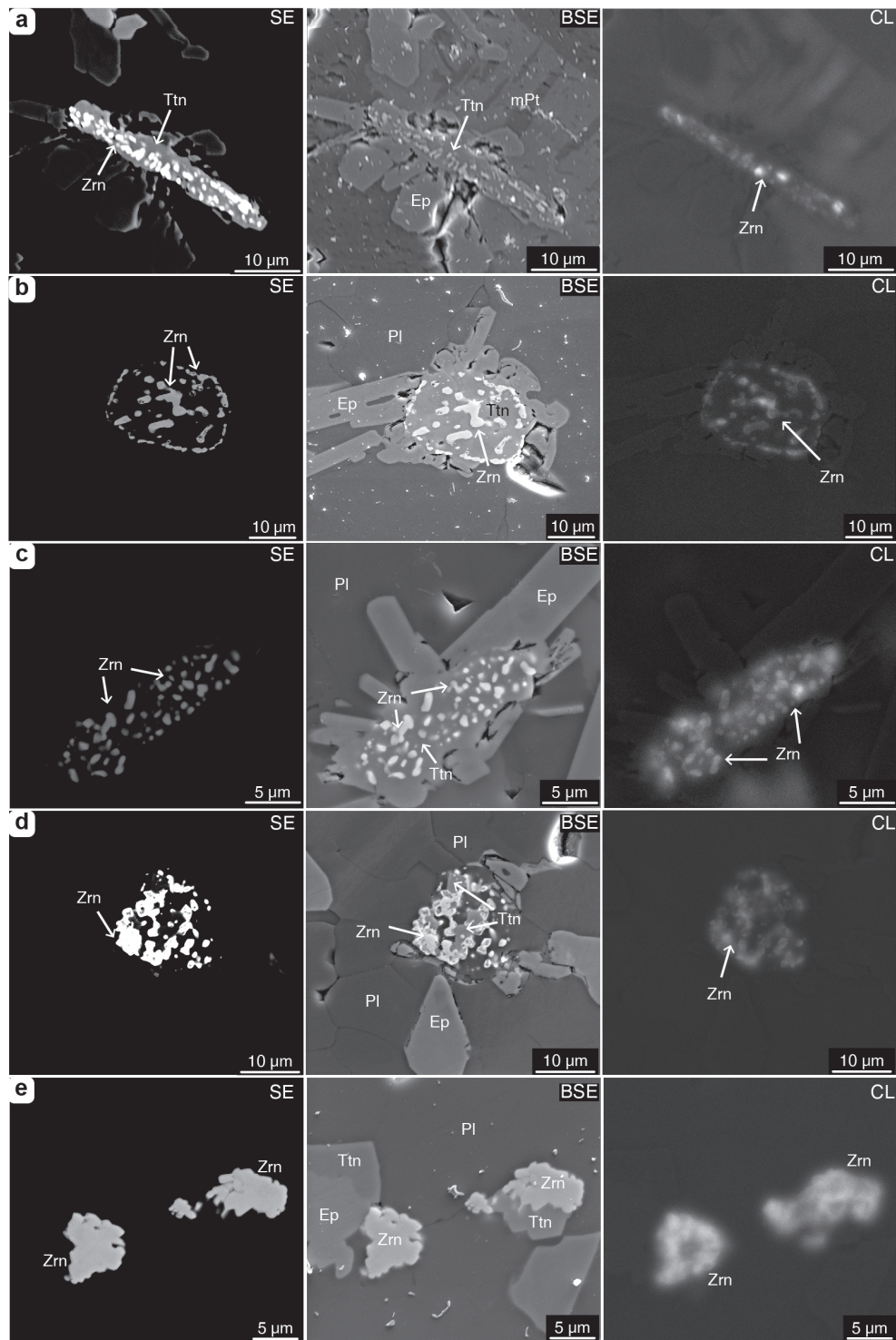
Figure 4. Titanite–zircon intergrowths in metamorphosed syenodiorite **(a–b, d–e)** and syenite **(c)**. Images show textural variations in secondary electron (SE), backscatter electron (BSE), and cathodoluminescence (CL) images. Mineral abbreviations as in Figs. 2 and 3; Ep, epidote–clinozoisite; Ttn, titanite. See main text for descriptions.

Table 3. Chemical compositions of zirconolite and stoichiometry for the empirical formula. The analysed zirconolite crystals are shown in Fig. 3d (analysis Zrc 64_1) and Fig. 5 (analyses Zrc 24_2 and Zrc 24_3).

	Composition (wt %)				Atoms in formula on the basis of 8 cations and 14 O atoms		
Analysis	Zrc 24_2	Zrc 24_3	Zrc 64_1	Analysis	Zrc 24_2	Zrc 24_3	Zrc 64_1
MgO	0.08	0.08	0.04	Mg	0.02	0.02	0.01
Al_2O_3	0.32	0.35	2.43	Al	0.05	0.05	0.37
SiO_2	0.32	0.27	4.15	Si	0.04	0.04	0.53
CaO	9.58	9.27	8.45	Ca	1.34	1.3	1.16
TiO_2	33.82	34.56	28.29	Ti	3.32	3.4	2.73
FeO*	0.49	0.96	1.82	Fe^{2+}	0.05	0.11	0.2
Fe_2O_3*	6.1	5.58	5.66	Fe^{3+}	0.6	0.55	0.55
Y_2O_3	2.7	2.91	0.11	Y	0.2	0.2	0.01
ZrO_2	31.45	30.56	32.84	Zr	2	1.95	2.06
Nb_2O_5	0.23	0.19	0.28	Nb	0.01	0.01	0.02
La_2O_3	0.24	0.21	0.67	La	0.01	0.01	0.03
Ce_2O_3	2.53	2.59	3.93	Ce	0.12	0.12	0.19
Pr_2O_3	0.56	0.46	0.65	Pr	0.03	0.02	0.03
Nd_2O_3	2.21	2.66	1.77	Nd	0.1	0.12	0.08
Sm_2O_3	0.56	0.48	0.04	Sm	0.03	0.02	0.002
Eu_2O_3	0.11	0.04	0.19	Eu	0.01	0.002	0.01
Gd_2O_3	0.7	0.68	0.36	Gd	0.03	0.03	0.02
Dy_2O_3	0.47	0.36	bd	Dy	0.02	0.02	bd
Ho_2O_3	0.08	bd	0.12	Ho	0.003	bd	0.01
Er_2O_3	0.29	0.28	0.08	Er	0.01	0.01	0.003
Tm_2O_3	0.03	0.14	0.12	Tm	0.001	0.01	0.01
Yb_2O_3	0.22	0.29	0.1	Yb	0.01	0.01	0.004
Lu_2O_3	0.05	0.02	bd	Lu	0.002	0.001	bd
Total	93.14	92.94	92.10	Total	7.99	8.01	8.01
FeO_{eq}	5.98	5.90	6.91	ΣREE	0.56	0.58	0.38

Note: weight percentage (wt %) values for FeO* and $Fe_2O_3^*$ represent a stoichiometric recalculation from FeO_{eq} (measured value); bd denotes below detection.

REE, and minor bivalent cations for 2 apfu in the [VIII]M site. The [VII]M site is filled with Zr for 2 apfu, and [IV, V, VI]M sites are filled with Ti, Nb, and Fe^{3+} (and additional trivalent cations) for 4 apfu. Thus, the simplified formula may be expressed as $(Ca, REE)_2Zr_2^{VI}Ti_3^{IV\,V}(Ti, Nb, Fe^{3+})O_{14}$.

EBSD analysis was also performed on the largest (12 μm long) zirconolite crystal (Fig. 5), aiming to constrain the crystal structure. However, the analysis yielded no Kikuchi pattern for indexation of the crystal structure of zirconolite. During analysis, the Kikuchi patterns were non-existent or indistinct (see Supplement, Fig. S2). The EBSD results were thus inconclusive as a majority of the indexing resulted in zero solutions or yielded too high mean angular deviation values of > 1°.

6 Discussion

In addition to zircon, the rocks within the Vaggeryd syenite complex host the accessory minerals baddeleyite, zircono-

lite, and srilankite, likely due to their relative undersaturation in silica ($SiO_2 < 55$ % and absence of free quartz) and their Fe–Ti-rich and Zr-rich (> 180 ppm) bulk composition (see Supplement, Table S1). The mineral and textural relations between the near-pristine igneous and the gradually recrystallised syenodiorite varieties indicate that the intergrowths of titanite and zircon are the product of the breakdown of igneous zirconolite. As discussed below (Sect. 6.3), the production of metamorphic zircon and titanite depends on the supply of SiO_2 from the consumption of the igneous silicates.

6.1 Formation of the igneous Zr minerals

The coexisting magmatic zirconolite, baddeleyite, and zircon, documented in the near-pristine igneous syenodiorite, were likely formed during late-stage crystallisation from Zr-saturated melts (cf. Söderlund et al., 2005; Schaltegger and Davies, 2017). The crystallisation of the magmatic accessory phases was controlled by the relative activities of Si and Zr. Baddeleyite can crystallise before zircon when the magma reaches Zr saturation before silica saturation (Schaltegger
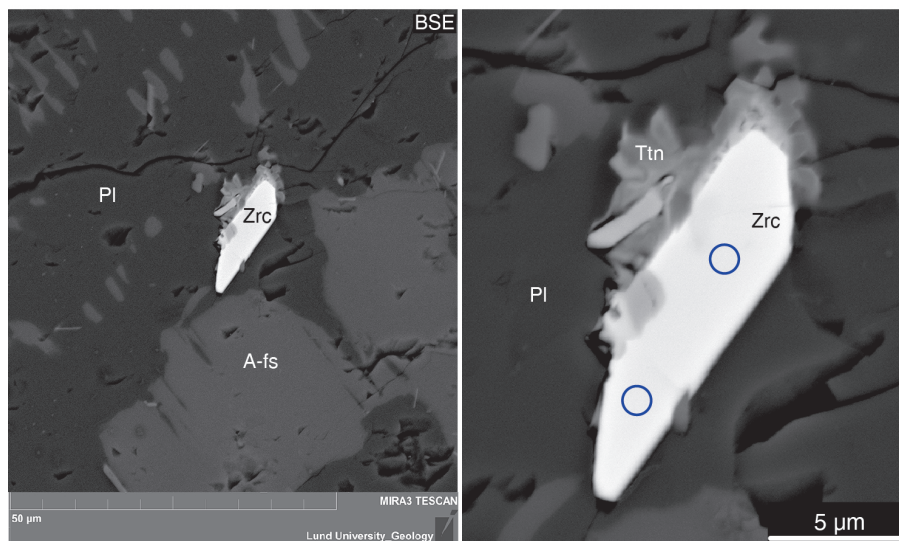
Figure 5. Backscatter electron image of one of two $> 5\,\mu m$ zirconolite crystals in near-pristine igneous syenodiorite (Fig. 2a, c, e–f). Closeup view indicating two EPMA spots (blue circles mark Zrc 24_2 and Zrc 24_3 in Table 3).

and Davies, 2017). As a consequence, the uptake of Zr by baddeleyite may later be followed by zircon growth. Additionally, the presence of two textural types of igneous zircon in one sample hints at a magmatic system with the recharge of melts of different syenitic compositions.

The coexistence of Zr-bearing phases has been reported from alkaline and mafic intrusions such as gabbro and anorthosite (e.g. Davidson and van Breemen, 1988; Heaman and LeCheminant, 1993; Scoates and Chamberlain, 1995; Rasmussen and Fletcher, 2004; Beckman et al., 2017, 2014). In silica-undersaturated syenitic intrusions, baddeleyite is found as an accessory mineral in association with different combinations of zirconolite, titanite, calcite, rutile, and zircon in the presence of a pure CO_2 fluid phase (Lumpkin, 1999). Moreover, Lumpkin (1999) argues that Fe and Ti incorporation into the chemical system broadens the stability field of baddeleyite and may explain the coexistence of baddeleyite and zircon. This may also be the case for coexistence with Fe-rich zirconolite. As the minute inclusions of baddeleyite in zirconolite were observed only in two crystals, without evidence of dissolution and/or replacement, the relationship between both minerals is interpreted as cogenetic. Nevertheless, in contrast to more coarsely sized baddeleyite that is widely distributed in the rock, the zirconolite is typically hosted in the alkali-feldspar domains. This spatial relationship may indicate that zirconolite crystallised in locally supersaturated interstitial liquids near the alkali feldspar.

Alternative mechanisms that describe the formation of Zr oxides associated with zircon involve metasomatic reactions (e.g. Lewerentz et al., 2019; Tropper et al., 2007). During contact metamorphism in marbles, at metamorphic temperatures of 500–600 °C, the introduction of CO_2-bearing fluids promoted the replacement of baddeleyite by metamor-

phic zirconolite, and, as the Si activity increased, metamorphic zircon partly replaced the zirconolite (cf. Tropper et al., 2007). Lewerentz et al. (2019) demonstrate the formation of baddeleyite from the consumption of zircon in amphibolite-facies conditions, in silica-saturated rocks, caused by the ingress of a Ca-bearing fluid, which saturated the system in Ca. Spiridonov et al. (2019) suggested another mechanism involving the formation of zirconolite and baddeleyite via the dissolution of zircon xenocrysts in a shallow-level mafic magma enriched in Zr, REE, and Th or U. Although these three studies include evidence of the mineral relationships and petrogenetic sequences within these rocks, there are no textural indications of the same processes in the rocks investigated here. Except for a lower value for loss on ignition (LOI), the whole-rock composition of the near-pristine igneous syenodiorite matches that of its metamorphosed equivalents, indicating no external supply of Si, Ca, or other elements. Igneous zirconolite and baddeleyite are only preserved in the near-pristine igneous rock, and no relationships suggest that zirconolite replaces baddeleyite or vice versa.

6.2 Mineral characterisation of the igneous zirconolite

Natural zirconolite is rarely reported because of its dominant association with silica-undersaturated and alkaline rocks (e.g. Williams and Gieré, 1996; Gieré et al., 1998; Rasmussen and Fletcher, 2004). Our findings of pseudomorphs of zirconolite indicate that this mineral may be more common than generally assumed, although rarely identified due to its small size.

The composition of zirconolite in the Vaggeryd syenitoid can be described by the endmember $CaREEZr_2Ti_3Me^{3+}O_{14}$, with minor substitutions only. For example, the amounts

of Nb^{5+} are too low for two of the other endmembers (Table 1). The mineral chemistry is consistent with Fe-bearing zirconolite being poor in Al and Mg reported for silica-undersaturated syenitic rocks (Fowler and Williams, 1986; Williams and Gieré, 1996; Gieré et al., 1998). The charge-balanced stoichiometric formula calculation (based on 8 cations and 14 O atoms) indicates that most of the total Fe (6.1 wt %–7.9 wt %) corresponds to Fe_2O_3 (5.6 wt %–6.1 wt %), which would hint at a high oxidation state during the late stage of crystallisation. However, this indication should be taken with caution because the calculation is sensitive to the weight percentage totals.

Although the zirconolite composition in the syenodiorite is closest to zirconolite-*3O* (cf. Bayliss et al., 1989; Spiridonov et al., 2019; Haifler et al., 2021) and the analogous polytype stefanweissite (Chukanov et al., 2019), the whole-grain EBSD map of the selected zirconolite crystal resulted in an extremely low contrast (black colour) image that indicates no patterns to be indexed for any mineral phase or other zirconolite polytype. The inability to determine a crystalline phase in this study may be a consequence of either immiscible intergrowths of zirconolite-like phases (e.g. zirkelite or zirconolite polytypes) during the igneous crystallisation or loss of crystallinity due to metamictisation. The most reasonable explanation for the lack of electron backscatter diffraction patterns is the amorphisation of the crystal. However, the analytical data in this study do not provide information to determine the cause of amorphisation. Further crystallographic analysis might ascertain the microstructural complexities of this mineral, but that is beyond the scope of this paper.
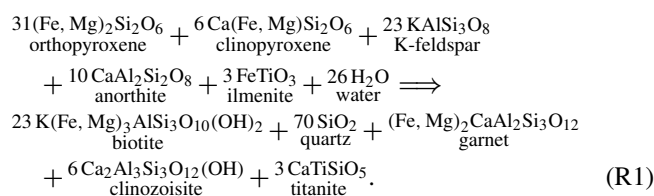
6.3 Metamorphic zircon-forming reactions

The formation of metamorphic zircon by the reaction of baddeleyite with a silica-bearing aqueous fluid has been documented in mafic rocks within a wide range of pressure and temperature (P–T) conditions (Davidson and van Breemen, 1988; Lumpkin, 1999; Söderlund et al., 2005; Beckman et al., 2017; Beckman and Möller, 2018). Commonly, remnants of baddeleyite crystals are surrounded by polycrystalline zircon coronas. Metamorphic zircon-forming reactions from other Zr-bearing accessory minerals, specifically zirconolite, are less commonly discussed but have been reported by Pan (1997) and Pohlner et al. (2020). Under subgreenschist conditions, the breakdown of zirconolite may involve changes by dissolution, alteration, and replacement (Gieré et al., 1998).

In the melanocratic syenodiorite and syenite studied here, tiny epidote–clinozoisite inclusions in the mesoperthite (10–30 µm, seen at high magnification, e.g. Fig. 4) are formed at the beginning of the metamorphic recrystallisation of a ternary feldspar that initially was richer in Ca. The main metamorphic mineral assemblages of the deformed (and undeformed) rocks, in particular the stability of epidote–clinozoisite and albite-rich plagioclase, bear witness to the
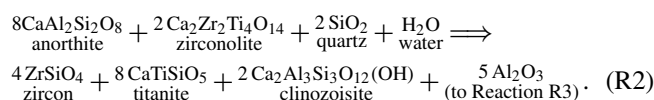
reactions taking place under epidote–amphibolite conditions (supported by P–T estimates reported in Urueña and Möller, 2023). During metamorphic recrystallisation, the anhydrous mineral paragenesis in the near-pristine igneous syenodiorite was transformed into a mineral assemblage in which most ferromagnesian minerals are hydrous (biotite and epidote–clinozoisite). Thus, the mineral reactions, including the formation of zircon from Zr oxides, represent a specific stage during regional metamorphism when the influx of hydrous fluid associated with deformation triggered the breakdown of the (metastable) igneous minerals to form the metamorphic assemblage.

A general reaction can be balanced, which involves the main minerals in the near-pristine syenodiorite and is dependent on the introduction of hydrous fluid (Urueña and Möller, 2023):

$$\underset{\text{orthopyroxene}}{31(Fe,Mg)_2Si_2O_6} + \underset{\text{clinopyroxene}}{6\,Ca(Fe,Mg)Si_2O_6} + \underset{\text{K-feldspar}}{23\,KAlSi_3O_8}$$
$$+ \underset{\text{anorthite}}{10\,CaAl_2Si_2O_8} + \underset{\text{ilmenite}}{3\,FeTiO_3} + \underset{\text{water}}{26\,H_2O} \Longrightarrow$$
$$\underset{\text{biotite}}{23\,K(Fe,Mg)_3AlSi_3O_{10}(OH)_2} + \underset{\text{quartz}}{70\,SiO_2} + \underset{\text{garnet}}{(Fe,Mg)_2CaAl_2Si_3O_{12}}$$
$$+ \underset{\text{clinozoisite}}{6\,Ca_2Al_3Si_3O_{12}(OH)} + \underset{\text{titanite}}{3\,CaTiSiO_5}. \tag{R1}$$
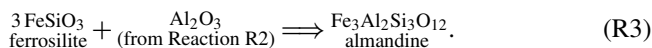
The breakdown of the igneous minerals (i.e. dominantly feldspars and orthopyroxene, Reaction 1) released Si (quartz) that was important for the formation of zircon from baddeleyite and zirconolite, and the Ca from calcic plagioclase component was used for the formation of metamorphic clinozoisite, titanite, and garnet. The production of biotite and clinozoisite from the dry pyroxene-bearing igneous assemblage necessarily involved the introduction of H_2O. This is also corroborated by the higher LOI values for the metamorphosed rocks than for the near-pristine igneous (Supplement, Table S1).

The breakdown of zirconolite into metamorphic zircon and titanite is a mineral reaction that is significantly subordinate in volume to that of the major minerals (Reaction 1) but which was also a consequence of the metamorphism in epidote–amphibolite-facies conditions. It can be described by the following simplified reaction:

$$\underset{\text{anorthite}}{8\,CaAl_2Si_2O_8} + \underset{\text{zirconolite}}{2\,Ca_2Zr_2Ti_4O_{14}} + \underset{\text{quartz}}{2\,SiO_2} + \underset{\text{water}}{H_2O} \Longrightarrow$$
$$\underset{\text{zircon}}{4\,ZrSiO_4} + \underset{\text{titanite}}{8\,CaTiSiO_5} + \underset{\text{clinozoisite}}{2\,Ca_2Al_3Si_3O_{12}(OH)} + \underset{\text{(to Reaction R3)}}{5\,Al_2O_3}. \tag{R2}$$

In Reaction (R2), SiO_2 (probably in aqueous solution) is provided from the bulk metamorphic reaction, Reaction (R1). The close spatial relationship with clinozoisite (epidote in Fig. 4) also suggests that this reaction took place during the infiltration of hydrous fluid. The products of Reaction (R2) indicate a Zrn / Ttn ratio of 1/2, which is consistent with the predominance of titanite over zircon in the pseudomorphs (e.g. Fig. 4a–d). Elements such as REE, Nb, and Fe^{3+} hosted in zirconolite are likely incorporated into clinozoisite, garnet, and other accessory phases. Reaction (R2) produces an excess of Al_2O_3 which necessarily was taken up by garnet

(simplified reaction, Reaction R3):

$$\underset{\text{ferrosilite}}{3\,FeSiO_3} + \underset{\text{(from Reaction R2)}}{Al_2O_3} \Longrightarrow \underset{\text{almandine}}{Fe_3Al_2Si_3O_{12}}. \tag{R3}$$

It is emphasised that igneous zircon crystals in the most deformed varieties lack textures that could suggest metamorphic dissolution and recrystallisation of the igneous zircon crystals, e.g. embayments or overgrowths. The polycrystalline zircon textures and the thin zircon rims around baddeleyite (Figs. 3, 4) suggest that metamorphic zircon formed from the consumption of baddeleyite and zirconolite. The result is that metamorphic zircon and igneous zircon are both present in the metamorphosed syenodiorite.

The formation of metamorphic zircon and titanite after zirconolite was first described by Pan (1997) from volcano-sedimentary rocks in Manitouwadge, Ontario (Canada), which underwent metamorphism and anatexis in high-grade conditions. Textural relationships within pseudomorphs attest to the breakdown reaction, Reaction (R4), of zirconolite to zircon + titanite + rutile, resulting in high contents of Nb and REE in the product minerals:

$$CaZrTi_2O_7 + 2Si^{4+} + 4O^{2-} \Longrightarrow$$
$$ZrSiO_4 + CaTiSiO_5 + TiO_2. \tag{R4}$$
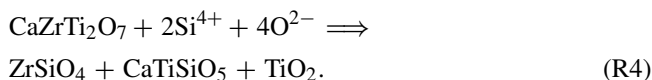
This transformation of zirconolite to metamorphic zircon + titanite + rutile was observed in rocks that underwent metamorphism in high-pressure upper-amphibolite-facies to granulite-facies conditions (Pan, 1997). In the syenodioritic rocks studied herein, rutile is absent and epidote present, which suggests that Reaction (R2) is representative of epidote–amphibolite-facies conditions.

7 Conclusions

In the syenitoid rocks described in this study, the formation of titanite + zircon after zirconolite took place during metamorphism under epidote–amphibolite-facies conditions and was associated with the breakdown of igneous ternary feldspar and orthopyroxene. The field relationships and the formation of hydrous ferromagnesian phases (and increase in bulk LOI) suggest that this metamorphic transformation was triggered by hydrous fluid infiltration associated with ductile deformation.

Titanite + zircon intergrowths, typically titanite speckled with micrometre-sized zircon and, less commonly, polycrystalline aggregates, are characteristic pseudomorphs of zirconolite. The precise reaction for the formation of metamorphic titanite + zircon intergrowths will depend on the whole-rock composition and the pressure–temperature conditions during metamorphism. However, in all cases, analogous to the formation of metamorphic zircon after baddeleyite, it depends on the release of silica from the breakdown of silicate minerals in the rock.

The formation of metamorphic zircon in silica-undersaturated rocks takes place during the breakdown of precursor igneous Zr oxides such as baddeleyite and/or zirconolite. Metamorphic titanite–zircon intergrowths represent pseudomorphs after igneous zirconolite, which are analogous with polycrystalline zircon pseudomorphs after igneous baddeleyite. These textural relationships allow the linkage of the metamorphic zircon formation and a regional metamorphic event.

References

Andersson, J.: U–Pb zircon geochronology of granitic and syenitoid rocks across the southern part of the Sveconorwegian orogen, SGU-rapport 2012, 14, 27 pp., http://resource.sgu.se/produkter/sgurapp/s1214-rapport.pdf (last access: 14 September 2023), 2012.

Ask, R.: Single zircon evaporation Pb–Pb ages from the Vaggeryd syenite and dolerites in the SE part of the Sveconorwegian orogen, Småland, S Sweden, GFF, 118, 8–8, https://doi.org/10.1080/11035899609546267, 1996.

Austrheim, H.: Eclogitization of lower crustal granulites by fluid migration through shear zones, Earth Planet. Sc. Lett., 81, 221–232, https://doi.org/10.1016/0012-821X(87)90158-0, 1987.

Austrheim, H.: Fluid and deformation induced metamorphic processes around Moho beneath continent collision zones: Examples from the exposed root zone of the Caledonian mountain belt, W-Norway, Tectonophysics, 609, 620–635, https://doi.org/10.1016/J.TECTO.2013.08.030, 2013.

Bayliss, P., Mazzi, F., Munno, R., and White, T. J.: Mineral nomenclature: zirconolite, Mineral. Mag., 53, 565–569, https://doi.org/10.1180/MINMAG.1989.053.373.07, 1989.

Beckman, V. and Möller, C.: Prograde metamorphic zircon formation in gabbroic rocks: The tale of microtextures, J. Metamorph. Geol., 36, 1221–1236, https://doi.org/10.1111/jmg.12443, 2018.

Beckman, V., Möller, C., Söderlund, U., Corfu, F., Pallon, J., and Chamberlain, K. R.: Metamorphic zircon formation at the transition from gabbro to eclogite in Trollheimen–Surnadalen, Norwegian Caledonides, Geol. Soc. Lond. Spec. Publ., 390, 403–424, https://doi.org/10.1144/SP390.26, 2014.

Beckman, V., Möller, C., Söderlund, U., and Andersson, J.: Zircon growth during progressive recrystallization of Gabbro to Garnet Amphibolite, Eastern Segment, Sveconorwegian orogen, J. Petrol., 58, 167–188, https://doi.org/10.1093/petrology/egx009, 2017.

Bingen, B., Austrheim, H., and Whitehouse, M. J.: Ilmenite as a Source for Zirconium during High-grade Metamorphism? Textural Evidence from the Caledonides of Western Norway and Implications for Zircon Geochronology, J. Petrol., 42, 355–375, https://doi.org/10.1093/PETROLOGY/42.2.355, 2001.

Carlier, G. and Lorand, J. P.: Zr-rich accessory minerals (titanite, perrierite, zirconolite, baddeleyite) record strong oxidation associated with magma mixing in the south Peruvian potassic province, Lithos, 104, 54–70, 2008.

Chukanov, N. V., Krivovichev, S. V., Pakhomova, A. S., Pekov, I. V., Schäfer, C., Vigasina, M. F., and Van, K. V.: Laachite, $(Ca,Mn)_2Zr_2Nb2TiFeO_{14}$, a new zirconolite-related mineral from the Eifel volcanic region, Germany, Eur. J. Mineral., 26, 103–111, https://doi.org/10.1127/0935-1221/2013/0025-2343, 2014.

Chukanov, N. V., Zubkova, N. V., Britvin, S. N., Pekov, I. V., Vigasina, M. F., Schäfer, C., Ternes, B., Schüller, W., Polekhovsky, Y. S., Ermolaeva, V. N., and Pushcharovsky, D. Y.: Nöggerathite-(Ce), $(Ce,Ca)_2Zr_2(Nb,Ti)(Ti,Nb)_2Fe^{2+}O_{14}$, a New Zirconolite-Related Mineral from the Eifel Volcanic Region, Germany, Minerals, 8, 449, https://doi.org/10.3390/MIN8100449, 2018.

Chukanov, N. V., Zubkova, N. V., Pekov, I. V., Vigasina, M. F., Polekhovsky, Y. S., Ternes, B., Schüller, W., Britvin, S. N., and Pushcharovsky, D. Y.: Stefanweissite, $(Ca,REE)_2Zr_2(Nb,Ti)(Ti,Nb)_2Fe^{2+}O_{14}$, a new zirconolite-related mineral from the Eifel paleovolcanic region, Germany, Mineral. Mag., 83, 607–614, https://doi.org/10.1180/mgm.2018.171, 2019.

Davidson, A. and van Breemen, O.: Baddeleyite-zircon relationships in coronitic metagabbro, Grenville Province, Ontario: implications for geochronology, Contrib. Mineral. Petrol., 100, 291–299, https://doi.org/10.1007/BF00379740, 1988.

De Hoog, J. C. M. and Van Bergen, M. J.: Volatile-induced transport of HFSE, REE, Th and U in arc magmas: evidence from zirconolite-bearing vesicles in potassic lavas of Lewotolo volcano (Indonesia), Contrib. Mineral. Petrol., 139, 485–502, 2000.

Della Ventura, G., Bellatreccia, F., and Williams, C. T.: Zirconolite with significant REEZrNb(Mn, Fe)O_7 From a xenolith of the Laacher See Eruptive Center, Eifel Volcanic Region, Germany, Can. Mineral., 38, 57–65, https://doi.org/10.2113/GSCANMIN.38.1.57, 2000.

Droop, G. T. R.: A general equation for estimating Fe^{3+} concentrations in ferromagnesian silicates and oxides from microprobe analyses, using stoichiometric criteria, Mineral. Mag., 51, 431–435, https://doi.org/10.1180/MINMAG.1987.051.361.10, 1987.

Engvik, A. K., Austrheim, H., and Andersen, T. B.: Structural, mineralogical and petrophysical effects on deep crustal rocks of fluid-limited polymetamorphism, Western Gneiss Region, Norway, J. Geol. Soc. Lond., 157, 121–134, https://doi.org/10.1144/jgs.157.1.121, 2000.

Engvik, A. K., Austrheim, H., and Erambert, M.: Interaction between fluid flow, fracturing and mineral growth during eclogitization, an example from the Sunnfjord area, Western Gneiss Region, Norway, Lithos, 57, 111–141, https://doi.org/10.1016/S0024-4937(01)00037-8, 2001.

Fowler, M. B. and Williams, C. T.: Zirconolite from the Glen Dessarry Syenite; a comparison with other Scottish zirconolites, Mineral. Mag., 50, 326–328, https://doi.org/10.1180/minmag.1986.050.356.21, 1986.

Gieré, R.: Zirconolite, allanite and hoegbomite in a marble skarn from the Bergell contact aureole: implications for mobility of Ti, Zr and REE, Contrib. Mineral. Petrol., 93, 459–470, 1986.

Gieré, R., Williams, C. T., and Lumpkin, G. R.: Chemical characteristics of natural zirconolite, Swiss J. Geosci. Suppl., 78, 433–459, https://doi.org/10.5169/seals-59299, 1998.

Gyomlai, T., Yamato, P., and Godard, G.: Petrological study of an eclogite-facies metagranite from the Champtoceaux Complex

(La Picherais, Armorican Massif, France), Eur. J. Mineral., 35, 589–611, https://doi.org/10.5194/ejm-35-589-2023, 2023.

Haifler, J., Škoda, R., Filip, J., Larsen, A. O., and Rohlíček, J.: Zirconolite from Larvik Plutonic Complex, Norway, its relationship to stefanweissite and nöggerathite, and contribution to the improvement of zirconolite end-member systematics, Am. Mineral., 106, 1255–1272, https://doi.org/10.2138/AM-2021-7510, 2021.

Harley, S. L.: Mg-A1 yttrian zirconolite in a partially melted sapphirine granulite, Vestfold Hills, East Antarctica, Mineral. Mag., 58, 259–269, https://doi.org/10.1180/minmag.1994.058.391.08, 1996.

Heaman, L. M. and LeCheminant, A. N.: Paragenesis and U–Pb systematics of baddeleyite (ZrO_2), Chem. Geol., 110, 95–126, https://doi.org/10.1016/0009-2541(93)90249-I, 1993.

Jamtveit, B., Moulas, E., Andersen, T. B., Austrheim, H., Corfu, F., Petley-Ragan, A., and Schmalholz, S. M.: High Pressure Metamorphism Caused by Fluid Induced Weakening of Deep Continental Crust OPEN, Sci. Rep., 8, 17011, https://doi.org/10.1038/s41598-018-35200-1, 2018.

Johansson, L., Möller, C., and Söderlund, U.: Geochronology of eclogite facies metamorphism in the Sveconorwegian Province of SW Sweden, Precambrian Res., 106, 261–275, https://doi.org/10.1016/S0301-9268(00)00105-4, 2001.

Lewerentz, A., Harlov, D. E., Scherstén, A., and Whitehouse, M. J.: Baddeleyite formation in zircon by Ca-bearing fluids in silica-saturated systems in nature and experiment: resetting of the U–Pb geochronometer, Contrib. Mineral. Petrol., 174, 64, https://doi.org/10.1007/s00410-019-1600-8, 2019.

Lumpkin, G. R.: Physical and chemical characteristics of baddeleyite (monoclinic zirconia) in natural environments: an overview and case study, J. Nucl. Mater., 274, 206–217, https://doi.org/10.1016/S0022-3115(99)00066-5, 1999.

Mazzi, F. and Munno, R.: Calciobetafite (new mineral of the pyrochlore group) and related minerals from Campi Flegrei, Italy; crystal structures of polymignyte and zirkelite: comparison with pyrochlore and zirconolite, Am. Mineral., 68, 262–276, 1983.

Menegon, L., Pennacchioni, G., Malaspina, N., Harris, K., and Wood, E.: Earthquakes as Precursors of Ductile Shear Zones in the Dry and Strong Lower Crust, Geochem. Geophy. Geosy., 18, 4356–4374, https://doi.org/10.1002/2017GC007189, 2017.

Möller, C. and Andersson, J.: Metamorphic zoning and behaviour of an underthrusting continental plate, J. Metamorph. Geol., 36, 567–589, https://doi.org/10.1111/jmg.12304, 2018.

Möller, C., Andersson, J., Dyck, B., and Antal Lundin, I.: Exhumation of an eclogite terrane as a hot migmatitic nappe, Sveconorwegian orogen, Lithos, 226, 147–168, https://doi.org/10.1016/J.LITHOS.2014.12.013, 2015.

Nickolsky, M. S. and Yudintsev, S. V.: Electron Backscattered Diffraction for the Study of Matrices for Immobilization of Actinides Composed of the Murataite-Type Phases, Crystallogr. Reports, 66, 130–141, https://doi.org/10.1134/S1063774521010090, 2021.

Pan, Y.: Zircon and monazite forming metamorphic reactions at Manitouwadge, Ontario, Can. Mineral., 35, 105–123, 1997.

Piñán-Llamas, A., Andersson, J., Möller, C., Johansson, L., and Hansen, E.: Polyphasal foreland-vergent deformation in a deep section of the 1 Ga Sveconorwegian orogen, Precambrian Res.,

265, 121–149, https://doi.org/10.1016/j.precamres.2015.05.009, 2015.

Pohlner, J. E., Schmitt, A. K., Chamberlain, K. R., Davies, J. H. F. L., Hildenbrand, A., and Austermann, G.: Multimethod U–Pb baddeleyite dating: insights from the Spread Eagle Intrusive Complex and Cape St. Mary's sills, Newfoundland, Canada, Geochronology, 2, 187–208, https://doi.org/10.5194/GCHRON-2-187-2020, 2020.

Purtscheller, F. and Tessadri, R.: Zirconolite and baddeleyite from metacarbonates of the Oetzstal–Stubai Complex (northern Tyrol, Austria), Mineral. Mag., 49, 523–529, https://doi.org/10.1180/minmag.1985.049.353.05, 1985.

Pyatenko, Y. A. and Pudovkina, Z. V.: The lattice metric of $CaZrTi_2O_7$ crystals, Sov. Phys. Cryst., 9, 98–100, 1964.

Rasmussen, B. and Fletcher, I. R.: Zirconolite: A new U–Pb chronometer for mafic igneous rocks, Geology, 32, 785–788, https://doi.org/10.1130/G20658.1, 2004.

Schaltegger, U. and Davies, J. H. F. L.: Petrochronology of Zircon and Baddeleyite in Igneous Rocks: Reconstructing Magmatic Processes at High Temporal Resolution, Rev. Mineral. Geochem., 83, 297–328, https://doi.org/10.2138/RMG.2017.83.10, 2017.

Scoates, J. S. and Chamberlain, K. R.: Baddeleyite (ZrO_2) and zircon ($ZrSiO_4$) from anorthositic rocks of the Laramie anorthosite complex, Wyoming: Petrologic consequences and U–Pb ages, Am. Mineral., 80, 1317–1327, https://doi.org/10.2138/AM-1995-11-1222, 1995.

Söderlund, U. and Ask, R.: Mesoproterozoic bimodal magmatism along the protogine zone, S Sweden: Three magmatic pulses at 1.56, 1.22 and 1.205 Ga, and regional implications, Geologiska Föreningen i Stockholm, 128, 303–310, https://doi.org/10.1080/11035890601284303, 2006.

Söderlund, U., Jarl, L. G., Persson, P. O., Stephens, M. B., and Wahlgren, C. H.: Protolith ages and timing of deformation in the eastern, marginal part of the Sveconorwegian orogen, southwestern Sweden, Precambrian Res., 94, 29–48, https://doi.org/10.1016/S0301-9268(98)00104-1, 1999.

Söderlund, U., Isachsen, C. E., Bylund, G., Heaman, L. M., Patchett, P. J., Vervoort, J. D., and Andersson, U. B.: U–Pb baddeleyite ages and Hf, Nd isotope chemistry constraining repeated mafic magmatism in the Fennoscandian Shield from 1.6 to 0.9 Ga, Contrib. Mineral. Petrol., 150, 174–194, https://doi.org/10.1007/s00410-005-0011-1, 2005.

Spiridonov, E. M., Filimonov, S. V., Semikolennykh, E. S., Korotaeva, N. N., and Krivitskaya, N. N.: Zirconolite, Baddeleyite, Zircon, and Thorite of Island-Arc Quartz Gabbronorite-Dolerites of the Ayu-Dag Intrusive, Crimean Mountains, Moscow Univ. Geol. Bull., 73, 538–548, https://doi.org/10.3103/S0145875218060121, 2019.

Stephens, M. B., Bergström, U., and Wahlgren, C.-H.: Regional context and lithotectonic framework of the 1.1–0.9 Ga Sveconorwegian orogen, southwestern Sweden, in: Sweden: Lithotectonic Framework, Tectonic Evolution and Mineral Resources. Geological Society, London, Memoirs, Vol. 50, edited by: Stephens, M. B. and Bergman-Weihed, J., Geol. Soc. Lond., 337–349, https://doi.org/10.1144/m50-2018-17, 2020.

Troitzsch, U., Christy, A. G., and Ellis, D. J.: The crystal structure of disordered (Zr, Ti)O_2 solid solution including srilankite: evolution towards tetragonal ZrO_2 with increasing Zr, Phys. Chem.

Miner., 32, 504–514, https://doi.org/10.1007/s00269-005-0027-0, 2005.

Tropper, P., Harlov, D., Krenn, E., Finger, F., Rhede, D., and Bernhard, F.: Zr-bearing minerals as indicators for the polymetamorphic evolution of the eastern, lower Austroalpine nappes (Stubenberg Granite contact aureole, Styria, Eastern Alps, Austria), Lithos, 95, 72–86, https://doi.org/10.1016/j.lithos.2006.07.008, 2007.

Ulmius, J., Andersson, J., and Möller, C.: Hallandian 1.45 Ga high-temperature metamorphism in Baltica: P–T evolution and SIMS U–Pb zircon ages of aluminous gneisses, SW Sweden, Precambrian Res., 265, 10–39, 2015.

Urueña, C. and Möller, C.: Fluid-induced metamorphism and deformation at the eastern boundary of the Sveconorwegian Province, in: Metamorphism in the roots of mountain belts and its effect on rock technical properties: A case study of the Eastern Segment, Sveconorwegian orogen, edited by: Urueña, C., PhD thesis, Lund University, Sweden, 174 pp., ISBN 978-91-87847-72-1, 2023.

Wahlgren, C. H., Cruden, A. R., and Stephens, M. B.: Kinematics of a major fan-like structure in the eastern part of the Sveconorwegian orogen, Baltic Shield, south-central Sweden, Precambrian Res., 70, 67–91, https://doi.org/10.1016/0301-9268(94)90021-3, 1994.

Wang, N., Mao, Q., Zhang, T., Hao, J., and Lin, Y.: NanoSIMS and EPMA dating of lunar zirconolite, Prog. Earth Planet. Sci., 8, 1–8, 2021.

Whitney, D. L. and Evans, B. W.: Abbreviations for names of rock-forming minerals, Am. Mineral., 95, 185–187, https://doi.org/10.2138/am.2010.3371, 2010.

Williams, C. T. and Gieré, R.: Metasomatic zonation of REE in zirconolite from a marble skarn at the Bergell contact aureole (Switzerland/Italy), Schweiz. Mineral. Petrogr. Mitteil., 68, 133–140, 1988.

Williams, C. T. and Gieré, R.: Zirconolite: A Review of Localities Worldwide, and a Compilation of its Chemical Compositions, Bull. Nat. Hist. Museum Lond., 52, 1–24, 1996.

Zubkova, N. V., Chukanov, N. V., Pekov, I. V., Ternes, B., Schüller, W., Ksenofontov, D. A., and Pushcharovsky, D. Y.: The crystal structure of non-metamict Nb-rich zirconolite-3T from the Eifel paleovolcanic region, Germany, Zeitschrift für Krist.-Cryst. Mater., 233, 463–468, https://doi.org/10.1515/ZKRI-2017-2133, 2018.